The Astrophysical Journal, 734:45 (13pp), 2011 June 10 doi:10.1088/0004-637X/734/1/45

KINETIC VERSUS MULTI-FLUID APPROACH FOR INTERSTELLAR NEUTRALS IN THE HELIOSPHERE: EXPLORATION OF THE INTERSTELLAR MAGNETIC FIELD EFFECTS

Fathallah Alouani-Bibi[1], Merav Opher[1,2], Dimitry Alexashov[3], Vladislav Izmodenov[3,4], and Gabor Toth[5]
[1] Physics and Astronomy Department, George Mason University, Fairfax, VA, USA; alouani@physics.gmu.edu, mopher@bu.edu
[2] Astronomy Department, Boston University, Boston, MA, USA
[3] Space Research Institute (IKI) and Institute for Problems in Mechanics, Russian Academy of Science, Moscow, Russia
[4] Department of Aeromechanics and Gas Dynamics, Faculty of Mechanics, Lomonosov Moscow State University, Moscow, Russia
[5] Center for Space Environment Modeling, University of Michigan, MI, USA
Received 2010 December 3; accepted 2011 March 30; published 2011 May 24

ABSTRACT

We present a new three-dimensional (3D) self-consistent two-component (plasma and neutral hydrogen) model of the solar wind interaction with the local interstellar medium (LISM). This model (K-MHD) combines the magnetohydrodynamic treatment of the solar wind and the ionized LISM component with a kinetic model of neutral interstellar hydrogen (LISH). The local interstellar magnetic field ($B_{\rm LISM}$) intensity and orientation are chosen based on an early analysis of the heliosheath flows. The properties of the plasma and neutrals obtained using the K-MHD model are compared to previous multi-fluid and kinetic models. The new treatment of LISH revealed important changes in the heliospheric properties not captured by the multi-fluid model. These include a decrease in the heliocentric distance to the termination shock (TS), a thinner heliosheath, and a reduced deflection angle (θ) of the heliosheath flows. The asymmetry of the TS, however, seems to be unchanged by the kinetic aspect of the LISH.

Key words: ISM: atoms – ISM: kinematics and dynamics – magnetic fields – plasmas – shock waves – solar wind – Sun: heliosphere

Online-only material: color figures

1. INTRODUCTION

The interaction of the supersonic solar wind with the local interstellar medium (LISM) as the Sun travels through the galaxy results in the formation of the heliosphere in which our solar system is embedded (Axford 1972; Baranov 1990; Zank 1999; Pauls et al. 1995; Izmodenov & Kallenbach 2006). Within the termination shock (TS), the closest of the three heliospheric boundaries to the Sun, the solar wind is supersonic with latitudinal variations dependent on the solar cycle (McComas et al. 2006; Bzowski 2008; Izmodenov & Malama 2004). At the TS, the solar wind is decelerated to subsonic speeds and heated. The LISM and solar wind reach a pressure balance at the heliopause (HP), the second heliospheric boundary. Outside the HP, the LISM plasma and the frozen-in magnetic field drape over this boundary. The LISM neutrals on the other hand, not affected by the electromagnetic force, stream relatively freely through these heliospheric boundaries. Neutrals, mainly hydrogen, do, however, interact with the solar wind and LISM plasma through a resonant charge exchange (Lindsay & Stebbings 2005). This leads to a deceleration and a deflection of the interstellar neutrals outside the HP resulting in an enhanced density structure, "the hydrogen wall" (Baranov & Malama 1993; Linsky & Wood 1996). The third heliospheric boundary, the bow shock (BS), is a result of a deceleration of the LISM outside the HP. For a strong interstellar magnetic field, however, we now believe a BS is absent (Izmodenov et al. 2009; Opher et al. 2009).

Voyager 1 (*V1*) and *Voyager 2* (*V2*) recently reached the TS (Stone et al. 2005, 2008), giving a new and unique perspective of that region. One of the major findings of these two missions was the so-called north–south asymmetry, referring to a 10 AU difference in the locations of the TS at *V1* and *V2*. This asymmetry is believed to originate outside the HP and is most likely due to an asymmetric magnetic pressure (Opher et al. 2006). Some of this asymmetry, we believe, to a lesser extent, is due to variations in the solar wind ram pressure during the period between *V1* and *V2* crossings.

The local interstellar magnetic field ($B_{\rm LISM}$) is the least known parameter of the LISM. A strong constraint on the orientation of $B_{\rm LISM}$ was established by the *SOHO*/SWAN observations (Lallement et al. 2005, 2010). These measurements showed a deflection of the hydrogen flow by $\sim 4^{\circ}$ relative to the helium flow. The latter is assumed to be unaffected by the crossing of the heliosphere owing to its negligible charge-exchange coupling with the heliospheric plasma. Most of the deflection of hydrogen takes place outside the HP. The *SOHO*/SWAN measured deflection has been interpreted as being due to the local interstellar magnetic field (Izmodenov et al. 2005; Pogorelov et al. 2008; Alouani-Bibi et al. 2010).

Extended numerical modeling has been dedicated to understanding the heliosphere formation and dynamic and reproducing some of the observations (Baranov & Malama 1993; Zank 1999; Linde et al. 1998; Myasnikov et al. 2000; Opher et al. 2006, 2007, 2009; Izmodenov et al. 2005, 2009; Malama et al. 2006; Ratkiewicz & Grygorczuk 2008; Pogorelov et al. 2008, 2009). These studies underscored the key role that neutral LISM, mainly hydrogen, plays in the heliosphere. Neutral hydrogen dominates the ionized component of the LISM in terms of number density ($n_{\rm H}/n_p \sim 3$). Therefore, the heliospheric asymmetry (Izmodenov et al. 2005; Opher et al. 2006, 2007; Pogorelov et al. 2008, 2009), the heliosheath size, and the inferred properties of $B_{\rm LISM}$ (Pogorelov et al. 2008, 2009; Opher et al. 2009; Izmodenov 2009) are expected to be strongly affected by the neutral LISM component.

In the heliosphere, the Knudsen number (the ratio of the charge-exchange mean free path to the scale length of the system) for neutral hydrogen is greater than 1 (e.g., Izmodenov et al. 2000). A full kinetic treatment of neutrals is therefore

needed. Solving the kinetic equation is computationally challenging and time consuming, and most often approximations are used. One of these approximations is the multi-Maxwellian model, whereby neutrals are represented by multi-fluid species. Each species reflects the peculiar thermodynamic properties of the plasma between adjacent heliospheric boundaries (Zank & Pauls 1996; Alexashov & Izmodenov et al. 2005; Opher et al. 2009). Notwithstanding the fact that the multi-fluid model is a good approximation for describing the main features of the heliosphere, it has some limitations (Alexashov & Izmodenov 2005) and most often the accuracy of the model depends on the number of neutral species considered. Kinetic–hydrodynamic coupling procedures, i.e., kinetic neutrals and hydrodynamic plasma, were introduced two decades ago, and have been successfully applied to different geometries and parameters of the solar wind and the LISM (Malama 1991; Baranov & Malama 1993; Müller et al. 2000; Izmodenov & Malama 2004; Izmodenov et al. 2005; Heerikhuisen et al. 2006).

Here, we extend our three-dimensional (3D) magnetohydrodynamic (MHD) multi-fluid model (MF-MHD; Opher et al. 2009) to include a kinetic treatment of neutrals. The kinetic model has been developed by the Moscow group (Malama 1991; Baranov & Malama 1993; Izmodenov & Malama 2004; Izmodenov et al. 2005). In this new framework, we analyze the effect of neutral LISM on the location and the asymmetry of the heliospheric boundaries as well as on the properties of the heliosheath flows. We compare the results from the new model (K-MHD) and previous data using multi-fluid (MF-MHD; Opher et al. 2009) and kinetic (A–I; Izmodenov et al. 2005; Alexashov & Izmodenov 2005) models.

The paper is structured as follows: Section 2 describes the two models used for neutrals, multi-fluid and kinetic, and the MHD–kinetic coupling procedure. The boundary values for the solar wind and the LISM, and the geometry of the problem are laid out in Section 3. The results and discussion are presented in Section 4. Conclusions are presented in Section 5.

2. MODELS

We use a 3D ideal MHD single-ion fluid model to describe both the solar wind and the ionized component of the LISM. This is done using BATS-R-US code (Powell et al. 1999; Toth et al. 2005). The governing equations for the ionized component and magnetic field are

$$\frac{\partial \rho}{\partial t} + \vec{\nabla}\cdot\left(\rho\,\vec{u}\right) = 0 \tag{1}$$

$$\frac{\partial(\rho\,\vec{u})}{\partial t} + \vec{\nabla}\cdot(\rho\,\vec{u}\otimes\vec{u}) + \vec{\nabla}\cdot\left(p^*\overleftrightarrow{I} - \frac{(\vec{B}\otimes\vec{B})}{\mu_0}\right) = \vec{S}_M \tag{2}$$

$$\frac{\partial E}{\partial t} + \vec{\nabla}\cdot(E\,\vec{u}) + \vec{\nabla}\cdot\left(p^*\,\vec{u} - \frac{(\vec{u}\cdot\vec{B})\,\vec{B}}{\mu_0}\right) = S_E \tag{3}$$

$$\frac{\partial \vec{B}}{\partial t} = \vec{\nabla}\times(\vec{u}\times\vec{B}) \tag{4}$$

$$E = \frac{1}{2}\rho u^2 + \frac{p}{(\gamma-1)} + \frac{B^2}{2\mu_0} \tag{5}$$

$$p^* = p + \frac{B^2}{2\mu_0}. \tag{6}$$

The terms S_M and S_E are the momentum and energy source terms due to the charge exchange between neutrals and ions. These terms are derived in McNutt et al. (1998) for a single neutral population. They represent the combined contribution to the ion's momentum and energy by each of the neutral species. Here we consider four neutral populations:

$$\vec{S}_M = \sum_{j=1}^{4} \rho_p \nu_{H(j)} \left(\vec{U}_{H(j)} - \vec{U}_p\right) \tag{7}$$

$$S_E = \sum_{j=1}^{4} \rho_p \nu_{H(j)} \left[\left(\frac{U_{H(j)}^2 - U_p^2}{2}\right) + \frac{U^*_{H(j)}}{U^*_{M,H(j)}}\left(V^2_{Th,H(j)} - V^2_{\mathrm{Th},p}\right)\right]. \tag{8}$$

The index "j" refers to the neutral species, $\nu_{H(j)} = n_H U^*_{M,H(j)}\sigma_{\mathrm{ChEx}}$ and σ_{ChEx} are the charge-exchange frequency and cross section (Lindsay & Stebbings 2005), respectively. The bulk and the thermal speeds of neutral species "j" and ions are $(U_{H(j)}, U_p)$ and $(V_{\mathrm{Th},H(j)}, V_{\mathrm{Th},p})$, respectively. The terms $(U^*_{H(j)}, U^*_{M,H(j)})$ are the characteristic speeds at which the charge-exchange cross section is evaluated (see Equations (62)–(64) in McNutt et al. 1998). The expression $\sigma_{\mathrm{ChEx}}(U^*_{M,H(j)})$ is used to calculate the momentum and energy, while $\sigma_{\mathrm{ChEx}}(U^*_{H(j)})$ is used for the mass conservation equation for neutrals:

$$U^*_{H(j)} = \sqrt{|U_{H(j)} - U_p|^2 + \frac{4}{\pi}\left(V^2_{\mathrm{th},H(j)} + V^2_{\mathrm{th},p}\right)} \tag{9}$$

$$U^*_{M,H(j)} = \sqrt{|U_{H(j)} - U_p|^2 + \frac{64}{9\pi}\left(V^2_{\mathrm{th},H(j)} + V^2_{\mathrm{th},p}\right)}. \tag{10}$$

There is no density source term in Equation (1), as the ion number density in a single-ion fluid model is unchanged under the charge-exchange process. In Equations (2) and (3), the radiation pressure and the gravity are assumed to perfectly cancel each other out. Ionization processes such as photoionization and electron-impact ionization are also neglected. These processes play a much lesser role than charge exchange at larger radii ($R > 30$ AU). Electron-impact ionization may play some role in the heliosheath. Unfortunately, a detailed description of the electron velocity distribution function is needed to correctly calculate the rate of this process (see Allais et al. 2005), which is beyond the scope of this paper.

For the neutral component, hydrogen, we use both the multi-fluid and the kinetic models. The multi-fluid treatment of neutrals assumes four neutral populations, each reflecting the properties of the plasma between the different heliospheric boundaries (see Figures 1(a) and 2(a) and (b)). An extended study of the heliosheath flows with the multi-fluid model and comparisons with *Voyager* data can be found in Opher et al. (2009).

The governing equations for neutrals in the multi-fluid model are

$$\frac{\partial \rho_{H(j)}}{\partial t} + \vec{\nabla}\cdot\left(\rho_{H(j)}\,\vec{w}\right) = S_{\rho,H(j)} \tag{11}$$

$$\frac{\partial(\rho_{H(j)}\,\vec{w})}{\partial t} + \vec{\nabla}\cdot(\rho_{H(j)}\,\vec{w}\otimes\vec{w}) + \vec{\nabla}\cdot\left(p_{H(j)}\overleftrightarrow{I}\right) = \vec{S}_{M,H(j)} \tag{12}$$

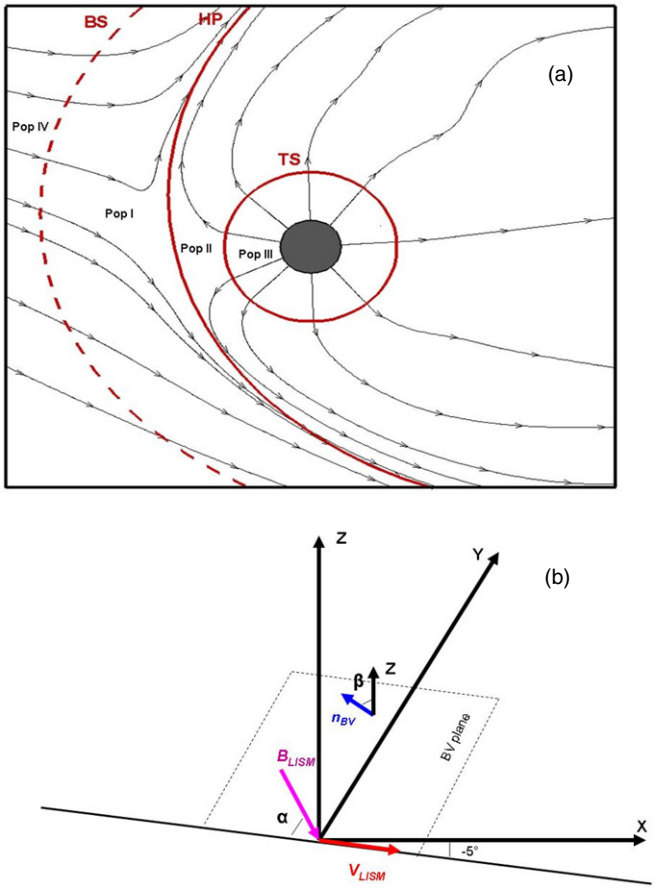

Figure 1. (a) Schematic representation, not to scale, of the heliospheric boundaries and the four neutral populations considered in the multi-fluid model. Numbers (I, II, III, IV) refer to the respective zones of each neutral population. Each neutral population "*i*" is generated through charge exchange only in its respective zone "*i*." When this population charge exchange in another zone "*j*," the created neutral population is "*j*." Here we used the same definitions as used in Opher et al. (2009). (b) The convention chosen for defining the angles (α) and (β). Angle (α) is the angle between $B_{\rm LISM}$ and local interstellar flow velocity $V_{\rm LISM}$; while (β) is the angle between the *BV* plane and the solar equatorial plane, respectively.

(A color version of this figure is available in the online journal.)

$$\frac{\partial E_{H(j)}}{\partial t} + \vec{\nabla} \cdot (E_{H(j)}\,\vec{w}) + \vec{\nabla} \cdot \left(p_{H(j)}\,\vec{w}\right) = S_{E,H(j)} \tag{13}$$

$$\chi = \begin{cases} 1 & \text{if } \vec{r}_{H(j)} \in \text{Zone}_{H(j)} \\ 0 & \text{otherwise} \end{cases} \tag{14}$$

$$S_{\rho,H(i)} = \chi \left(\sum_{j=1}^{4} \rho_p \nu_{H(j)} \right) - \rho_p \nu_{H(i)} \tag{15}$$

$$\vec{S}_{M,H(i)} = \chi \left(\sum_{j=1}^{4} \rho_p \nu_{H(j)} \vec{U}_p \right) - \rho_p \nu_{H(i)} \vec{U}_{H(i)} \tag{16}$$

$$S_{E,H(i)} = \chi \left(\sum_{j=1}^{4} \rho_p \nu_{H(j)} \left[\frac{U_p^2}{2} + \frac{U^*_{H(j)}}{U^*_{M,H(j)}} V^2_{Th,p} \right] \right) - \rho_p \nu_{H(i)} \left[\frac{U^2_{H(i)}}{2} + \frac{U^*_{H(i)}}{U^*_{M,H(i)}} V^2_{Th,H(i)} \right], \tag{17}$$

where "*i*" is the index of the neutral species. The function χ takes the value 1 when the neutral population (i) has its position vector inside its predefined source region (see below for the definition of these regions; Figures 1(a) and 2(a)). The terms ($S_{M,H(i)}$, $S_{E,H(i)}$) are the momentum and energy source terms for the neutral population (i) due to the charge exchange with ions. Under this formulation, where each population has a predefined source region, the number density of each population is not a conserved quantity while the total number density of all neutral species is.

To define the source region of each neutral population, an a priori assumption regarding the location of the TS and HP is needed. This assumption is based on the behavior of the plasma (density, temperature, bulk speed, and magnetic field) throughout the heliosphere. In other words, the source regions for neutrals are chosen based on MHD criteria.

The source region for the primary LISM neutrals (population IV), farther from the HP at the undisturbed LISM or beyond the BS in the case of a low-intensity $B_{\rm LISM}$, is defined as having magnetosonic Mach number $M_{\rm mag}$ and flow speed U as $M_{\rm mag} > 0.5$ and $U < 100$ km s^{-1}, respectively. The region between the BS and the HP, where the secondary LISM neutrals (population I) are produced through charge exchange with the LISM plasma, satisfies $M_{\rm mag} < 0.5$, $U < 100$ km s^{-1}, and $T < 10^5$ K. Population II is produced in the heliosheath, by charge exchange between the LISM neutrals and the shocked solar wind. This region is defined with characteristic subsonic speed with $M_{\rm mag} < 0.5$ and temperature $T > 10^5$ K. Population III is generated within the TS as a result of charge exchange between the LISM neutrals the supersonic solar wind.

The steady-state density distribution of these neutral populations is shown in Figures 2(a) and (b) and 3(a) and (b). Figure 2(a) portrays a 2D map of the density of each population, while Figure 2(b) shows the sum of all populations. The "hydrogen wall" structure is clearly visible in Figure 2(b). Radial density profiles, taken along the *X*-axis, in the upwind LISM flow direction, are shown in Figures 3(a) and (b).

The kinetic model of neutral hydrogen is based on the solution of the kinetic equation using the Monte Carlo method. Details of the model are presented in Malama (1991), Baranov & Malama (1993), Izmodenov & Malama (2004), and Izmodenov et al. (2005). The Boltzmann charge-exchange collision operator for neutrals, including the production and the ionization terms, is

$$S = -f_H(\vec{w}_H) \int |\vec{w}_H - \vec{w}_p| \sigma_{\rm ChEx} f_p(\vec{w}_p) d\vec{w}_p + f_p(\vec{w}_H) \times \int |\vec{u}_H - \vec{w}_H| \sigma_{\rm ChEx} f_p(\vec{u}_H) d\vec{u}_H - (\nu_{\rm ph} + \nu_{\rm imp}) f_H(\vec{w}_H), \tag{18}$$

where ($f_{\rm H}$, f_p) are the velocity distribution functions of neutrals and protons, respectively. In this model, the protons are represented by a Maxwellian distribution function, defined by the local plasma temperature, density, and bulk speed (n_p, T_p, U_p). These plasma parameters are taken as input from the MHD calculations at each kinetic–MHD iteration. The multi-component nature of the ionized component is not considered in this paper (see Malama et al. 2006; Chalov & Fahr 2010). Photoionization and electron-impact ionization terms in Equation (18), i.e., ($\nu_{\rm ph}$, $\nu_{\rm imp}$), are not taken into account in the kinetic model, as is the case in the mass conservation equation (Equation (1)) for the MHD model.

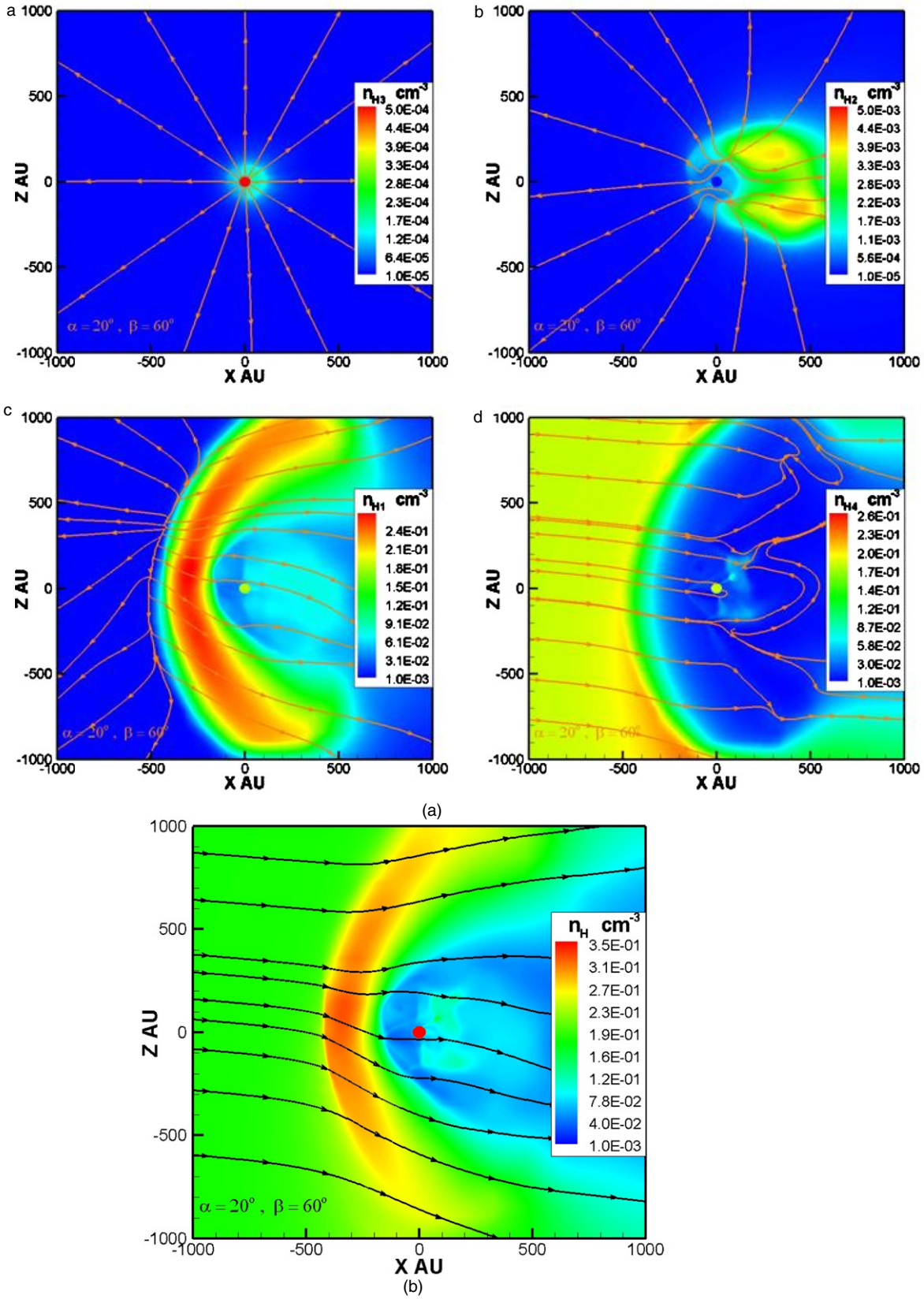

Figure 2. (a) Density map of neutral hydrogen, multi-neutral populations, (MF-MHD) model. The $B_{\rm LISM}$ intensity is 4.4 μG and its direction is defined by ($\alpha = 20^\circ$ and $\beta = 60^\circ$). The streamlines represent the velocity components (U_x, U_z) of each respective species. (b) Density map of neutral hydrogen, the sum of all populations, MF-MHD model. The $B_{\rm LISM}$ intensity is 4.4 μG and its direction is defined by ($\alpha = 20^\circ$ and $\beta = 60^\circ$). The streamlines represent the density-weighted velocity components (U_x, U_z) for the sum of all neutral species.

(A color version of this figure is available in the online journal.)

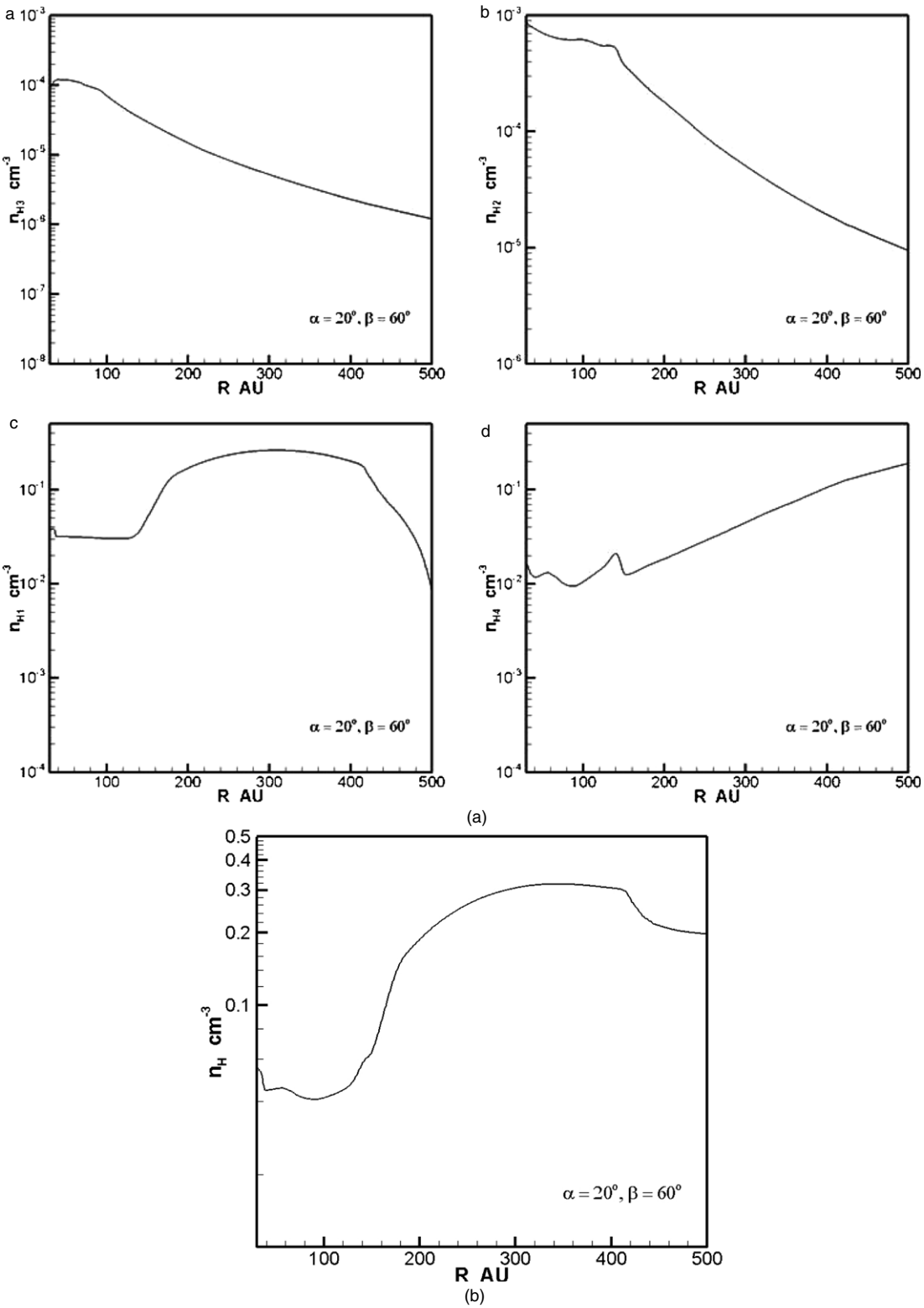

Figure 3. (a) Radial density profile, for multi-neutral populations, along the *X*-axis in the upwind LISM flow direction, MF-MHD model. The $B_{\rm LISM}$ intensity is 4.4 μG and its direction is defined by ($\alpha = 20^\circ$ and $\beta = 60^\circ$). (b) Radial density profile, for the sum of all populations, along the *X*-axis in the upwind LISM flow direction, MF-MHD model. The $B_{\rm LISM}$ intensity is 4.4 μG and its direction is defined by ($\alpha = 20^\circ$ and $\beta = 60^\circ$).

The steady-state solution with the K-MHD model is reached after a series of iterative steps. The initial phase, step 1, of this iterative process is achieving a steady-state solution for a given set of initial parameters of the LISM and the solar wind. The steady state is attained using a 3D MHD model with a multi-fluid (four neutral populations) description of neutrals. Both the LISM and the interplanetary magnetic fields are considered in our calculations. A Monte Carlo simulation of neutrals is carried out in step 2, using an updated proton distribution function in Equation (18). The distribution function is updated using local

plasma properties (n_p, T_p, U_p) taken from the MHD simulation. Thereafter, the generated kinetic neutrals quantities (n_H, T_H, U_H) are used in step 3 to calculate the momentum and energy source terms (S_M, S_E) for the ions. Therefore, Equations (7) and (8) are used from this point on in the iterative process, with a single kinetic population of neutrals. Therefore, Equations (11)–(18) are no longer updated. Step 3 is run for 500 time steps, before the output (n_p, T_p, U_p) is sent back for step 2. Steps 2 and 3 are repeated until a steady state is achieved between the kinetic neutrals and the MHD plasma. The coupling procedure converges quickly (after the fourth iteration). We use the same stationary adaptive mesh refinement (AMR) grid for the MHD and kinetic calculations. This is done to avoid any incremental interpolation errors due to the iterative process. The grid has been optimized to capture the main heliospheric features and the heliospheric boundaries.

3. SOLAR WIND AND LISM BOUNDARY VALUES

We consider a fully ionized solar wind plasma with number density, temperature, and flow speed given by $n_{\rm swp} = 8.7 \times 10^{-3}\,{\rm cm}^{-3}$, $T_{\rm swp} = 10^5$ K, and $V_{\rm swp} = 417\,{\rm km\,s}^{-1}$ (OMNI solar data, http://omniweb.gsfc.nasa.gov/). These values are assumed at the inner boundary, located at 30 AU from the Sun. The interplanetary magnetic field is given by the Parker solution (Parker 1961) at the inner boundary.

The solar wind parameters at 30 AU, inner boundary for the MHD model, are matched to those used in the kinetic model at 30 AU. The kinetic, Monte Carlo simulations have an inner boundary at 1 AU. The solar wind parameters are therefore extrapolated from 30 AU to 1 AU. The extrapolation assumes an adiabatic solar wind with a constant speed: $n_{\rm swp} \sim n_0/r^2$; $p_{\rm swp} \sim p_0/r^{2\gamma}$, $V_{\rm swp} = 417\,{\rm km\,s}^{-1}$.

At the outer boundary the LISM is considered with: $n_{{\rm LISM},p} = 0.06\,{\rm cm}^{-3}$, $n_{\rm LISM,H} = 0.18\,{\rm cm}^{-3}$, $T_{\rm LISM} = 6530$ K, and $V_{\rm LISM} = 26.4\,{\rm km\,s}^{-1}$ (Witte 2004; Möbius et al. 2004; Gloeckler et al. 2004). The intensity of the magnetic field carried by the LISM plasma is chosen as 4.4 μG, while the orientation of the field is varied. We define the orientation of the local interstellar magnetic field vector by two angles (α, β), where α is the angle between $B_{\rm LISM}$ and interstellar flow velocity $V_{\rm LISM}$ and β is the angle between the BV plane (the plane containing both $B_{\rm LISM}$ and $V_{\rm LISM}$) and the solar equatorial plane (see Figure 1(b)). The values assigned to these angles are $\alpha = 20^\circ$, 30° and $\beta = 60^\circ$, 80°, 90°, respectively. These are chosen based on a previous (MF-MHD) analysis of the heliosheath flows (Opher et al. 2009). The heliospheric asymmetry and the position of the TS are well reproduced with these orientations for a field intensity of 4.4 μG (Opher et al. 2009). The case of $\beta = 60^\circ$ was however less successful in describing the heliosheath flows. Nevertheless, it is important to mention that the value of β that most closely matches the inferred orientation of $B_{\rm LISM}$ from the *IBEX* data (McComas et al. 2009) is $\beta = 60^\circ$. This value has also been reported by Pogorelov et al. (2008) and Alouani-Bibi et al. (2010) to explain the hydrogen deflection in respect to helium (Lallement et al. 2005, 2010).

We adopt here the same convention for (α, β) as in Opher et al. (2009). The angle α is equal to zero for parallel $B_{\rm LISM}$ and $V_{\rm LISM}$ vectors, and increases from $V_{\rm LISM}$ counterclockwise toward $+Z$. The angle β is equal to zero at $+Y$ and increases counterclockwise from $+Y$ to $+Z$. The coordinate system is such that the Z-axis coincides with the solar rotation axis, and the X-axis lies on the plane spanned by the interstellar flow velocity vector $V_{\rm LISM}$ and the Z-axis. The $V_{\rm LISM}$ is at $\sim -5^\circ$ in respect to the X-axis. The Y-axis completes the orthogonal coordinate system. In this coordinate system, the interstellar flow velocity vector has coordinates of (26.3, 0, −2.3) km s^{-1}.

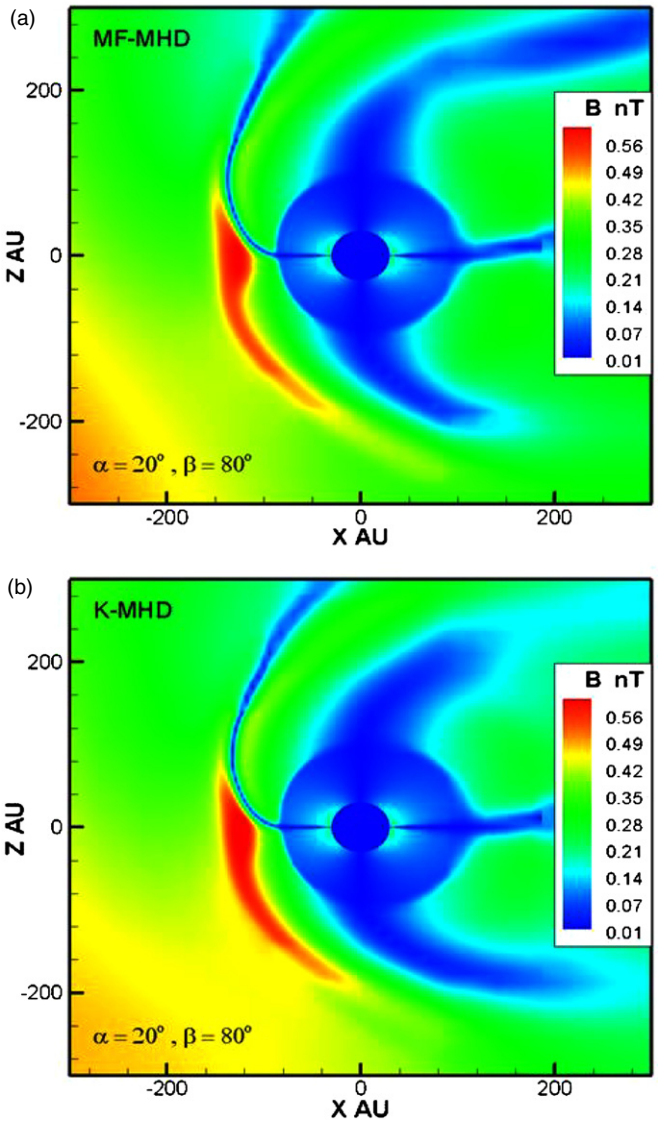

Figure 4. Two-dimensional intensity map of the magnetic field in the XZ plane for the two models: (a) MF-MHD and (b) K-MHD. The $B_{\rm LISM}$ intensity is 4.4 μG and its direction is defined by $\alpha = 20^\circ$ and $\beta = 80^\circ$.

(A color version of this figure is available in the online journal.)

We use an AMR grid with 11 levels of refinement (see Toth et al. 2005). The grid spans from −1500 AU to 1500 AU in each of the (X, Y, Z) direction. The spatial resolution varies from ∼0.7 AU near the inner boundary to ∼100 AU at the outer boundaries.

4. RESULTS AND DISCUSSION

We consider six different configurations of $B_{\rm LISM}$, each defined by a unique combination of (α, β). The values chosen for (α, β) are ($\alpha = 20^\circ$, 30° and $\beta = 60^\circ$, 80°, 90°), respectively. The $B_{\rm LISM}$ intensity is kept constant at 4.4 μG. The plasma properties described below are the number density, temperature, flow speed, and magnetic field.

The magnetic field intensity in the XZ plane is shown in Figures 4(a) and (b), for both the MF-MHD and the K-MHD

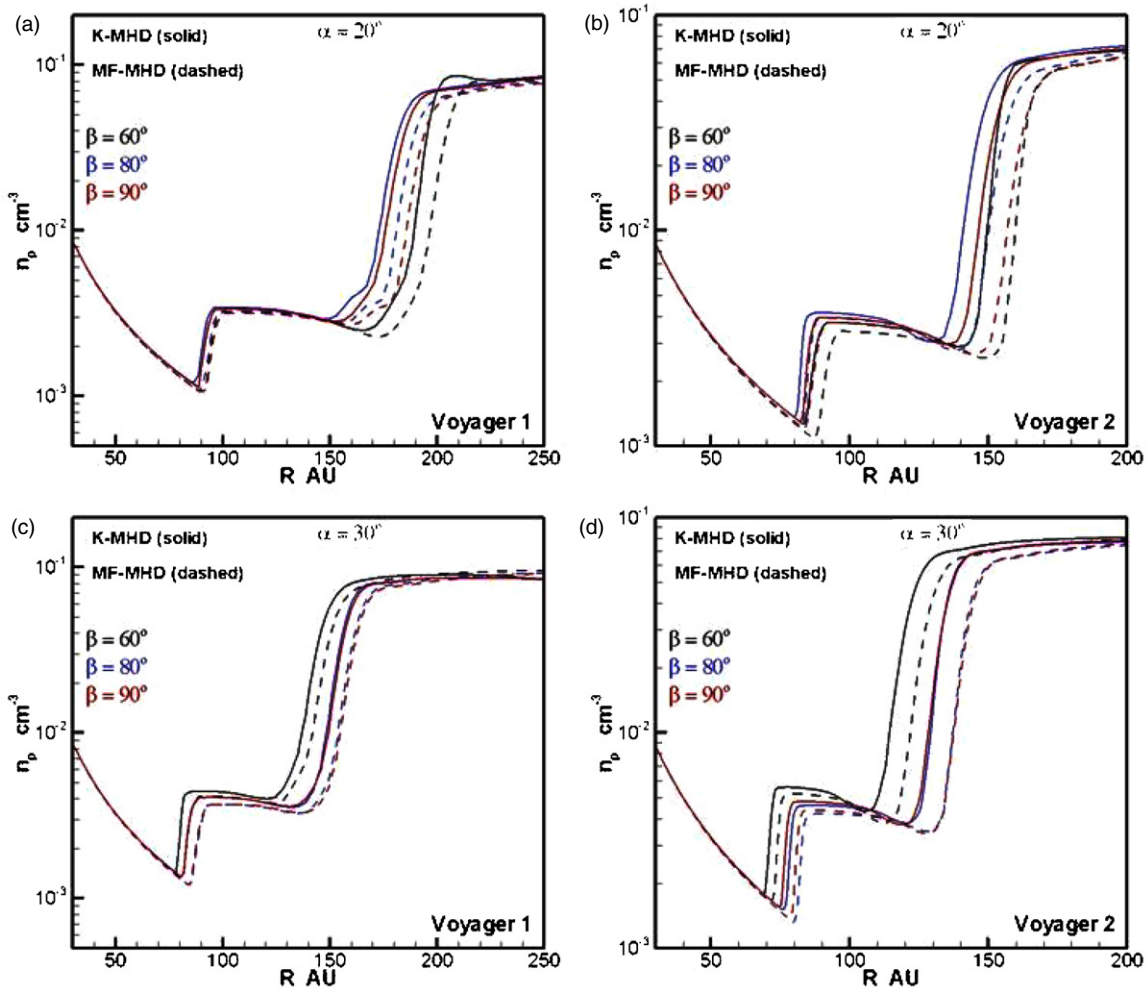

Figure 5. Protons number density profiles along the *V1* and *V2* trajectories. Neutral hydrogen is accounted for using two models: multi-fluid (dashed lines) and kinetic (solid lines). The $B_{\rm LISM}$ intensity is 4.4 μG. Data along the *V1* trajectory are shown in the left column, while the right column is for data along the *V2* trajectory. The upper row is for the cases with ($\alpha = 20^\circ$, $\beta = 60^\circ$, 80°, 90°). The lower row is for ($\alpha = 30^\circ$, $\beta = 60^\circ$, 80°, 90°).

(A color version of this figure is available in the online journal.)

models. For this particular case, the intensity and the direction of $B_{\rm LISM}$ are set to 4.4 μG and ($\alpha = 20^\circ$, $\beta = 80^\circ$), respectively. For this configuration, the same is in fact true for all the other configurations considered in this paper, the current sheet is directed northward. The 2D map (Figures 4(a) and (b)) shows variation in the field intensity between the two models used for neutrals. This intensity increase (Figure 4(b)) outside the HP is due to an unequal inward shift of the locations of the HP and the TS when the kinetic model is used to describe neutrals, as we will show later in the text. As a result, a net compression outside the HP takes place thus leading to an increase in the field intensity.

The protons' number density profiles along the *V1* and *V2* trajectories are presented in Figure 5. These profiles show a systematic decrease in the heliocentric distance to the TS and HP for the K-MHD model as compared with the MF-MHD model. This reduction is mostly sensitive to α, the angle between $B_{\rm LISM}$ and $V_{\rm LISM}$.

Magnetized shocks in a heliospheric environment have, in general, a characteristic thickness comparable to the thermal proton's gyroradius. This quantity is many orders of magnitude smaller than our grid resolution. We therefore introduce a concept of "mean value" to account for the illusiveness of the precise location of the heliospheric discontinuities in our calculations. The mean values for both TS and HP locations are calculated using the density and the velocity profiles. This is done by simply averaging the immediate upstream and downstream locations (see Table 1).

The mean heliocentric distance $\langle R_{\rm TS}\rangle$ to the TS is estimated for different values of (α, β) (see Table 1). For $\alpha = 20^\circ$, varying β by 30° ($\Delta\beta = 30^\circ$) induces a change in $\langle R_{\rm TS}\rangle$ of ~4 AU for the kinetic model and ~5.7 AU for the multi-fluid model. Similar estimates made for a constant β and a varying α showed a larger variation in $\langle R_{\rm TS}\rangle$. For $\beta = 60^\circ$, varying α by 10° ($\Delta\alpha = 10^\circ$) generated changes in $\langle R_{\rm TS}\rangle$ by ~16.3 AU and ~17.3 AU for the kinetic and multi-fluid models, respectively. The relative decrease in the mean heliocentric distance to the TS, $\langle R_{\rm TS}\rangle$, when neutrals are kinetic, has also been reported in other works (Pogorelov et al. 2008; Alexashov & Izmodenov 2005). Similar behavior is captured by the A–I model (see Figure 9) (Izmodenov et al. 2005; Alexashov & Izmodenov 2005). This reduction in $\langle R_{\rm TS}\rangle$ is a consequence of the solar win ram pressure decrease, as seen in velocity profiles (Figures 7(a) and (b)). This is due to an increase of the filtration factor (ratio of hydrogen number densities inside to the outside of the HP) in the kinetic model.

Table 1
The Calculated Locations of the Heliospheric Boundaries along *Voyager 1* (*V1*) and *Voyager 2* (*V2*) Trajectories

Direction of $B_{\rm LISM}$	MF-MHD						K-MHD					
	$\alpha = 20^\circ$ $\beta = 60^\circ$	$\alpha = 20^\circ$ $\beta = 80^\circ$	$\alpha = 20^\circ$ $\beta = 90^\circ$	$\alpha = 30^\circ$ $\beta = 60^\circ$	$\alpha = 30^\circ$ $\beta = 80^\circ$	$\alpha = 30^\circ$ $\beta = 90^\circ$	$\alpha = 20^\circ$ $\beta = 60^\circ$	$\alpha = 20^\circ$ $\beta = 80^\circ$	$\alpha = 20^\circ$ $\beta = 90^\circ$	$\alpha = 30^\circ$ $\beta = 60^\circ$	$\alpha = 30^\circ$ $\beta = 80^\circ$	$\alpha = 30^\circ$ $\beta = 90^\circ$
$R_{\rm TS}(V2)$ (AU)	91.95 ± 4.3	86.2 ± 3.6	87.9 ± 4.4	74.68 ± 3.2	83.26 ± 3.2	81.23 ± 2.9	87.82 ± 4.3	83.6 ± 3.7	85.18 ± 3.1	71.52 ± 2.7	78.86 ± 3.1	77.16 ± 2.7
$\Delta R_{\rm TS}(V1-V2)$ (AU)	2.65 ± 6.8	7.9 ± 6.2	7.82 ± 7.3	9.88 ± 5.3	6.17 ± 5.8	7.62 ± 5.9	4.56 ± 5.8	7.72 ± 6.1	7.02 ± 5.1	8.75 ± 3.5	6.04 ± 5.6	7.59 ± 5.3
$R_{\rm HP}(V2)$(AU)	165.63 ± 10.6	156.52 ± 12.3	162.55 ± 13.3	128.1 ± 12.5	142.56 ± 11	143.24 ± 12.1	153.03 ± 7.3	147.55 ± 12.8	152.04 ± 13.4	121.66 ± 13.3	138.93 ± 6	133.97 ± 12.3
$\Delta R_{\rm HP}(V1-V2)$(AU)	40.06 ± 19.2	32.01 ± 20	31.39 ± 20.2	23.89 ± 21.9	19.36 ± 18.9	19.12 ± 19.7	43.2 ± 14.4	33.27 ± 20	32.54 ± 19.6	23.15 ± 20.7	15.69 ± 15.4	21.81 ± 19.2
$L_{\rm HS}(V2)$(AU)	73.69 ± 11.4	70.33 ± 12.8	74.65 ± 14	53.42 ± 12.9	59.3 ± 11.4	62.01 ± 12.4	65.21 ± 8.5	63.95 ± 13.4	66.86 ± 13.8	50.15 ± 13.6	60.07 ± 6.74	56.81 ± 12.6
$\langle\Theta_{V2}\rangle$ $\tan^{-1}(V_N/V_T)$	−58.23	−66.92	−65.77	−66.52	−35.56	−54.8	−48.17	−62.37	−57.13	−62.08	−36.83	−50.46

Notes.
These data are for different configurations of the local interstellar magnetic field, defined by the angles (α, β). Two models are used for describing neutral hydrogen: multi-fluid (MF-MHD) and kinetic (K-MHD). RTS(*V2*): the mean heliocentric distance to the TS along *V2*; ΔRTS(*V1*−*V2*): the mean asymmetry of the TS between *V1* and *V2* crossing sites; RHP(*V2*): the mean heliocentric distance to the HP along *V2*; ΔRHS(*V1*−*V2*): the mean asymmetry of the HP between the extrapolated *V1* and *V2* crossing sites; LHS(*V2*): the mean heliosheath thickness along *V2* trajectory and $(\theta = \tan^{-1}(V_N/V_T))$: the deflection angle of the heliosheath flows along *V2*.

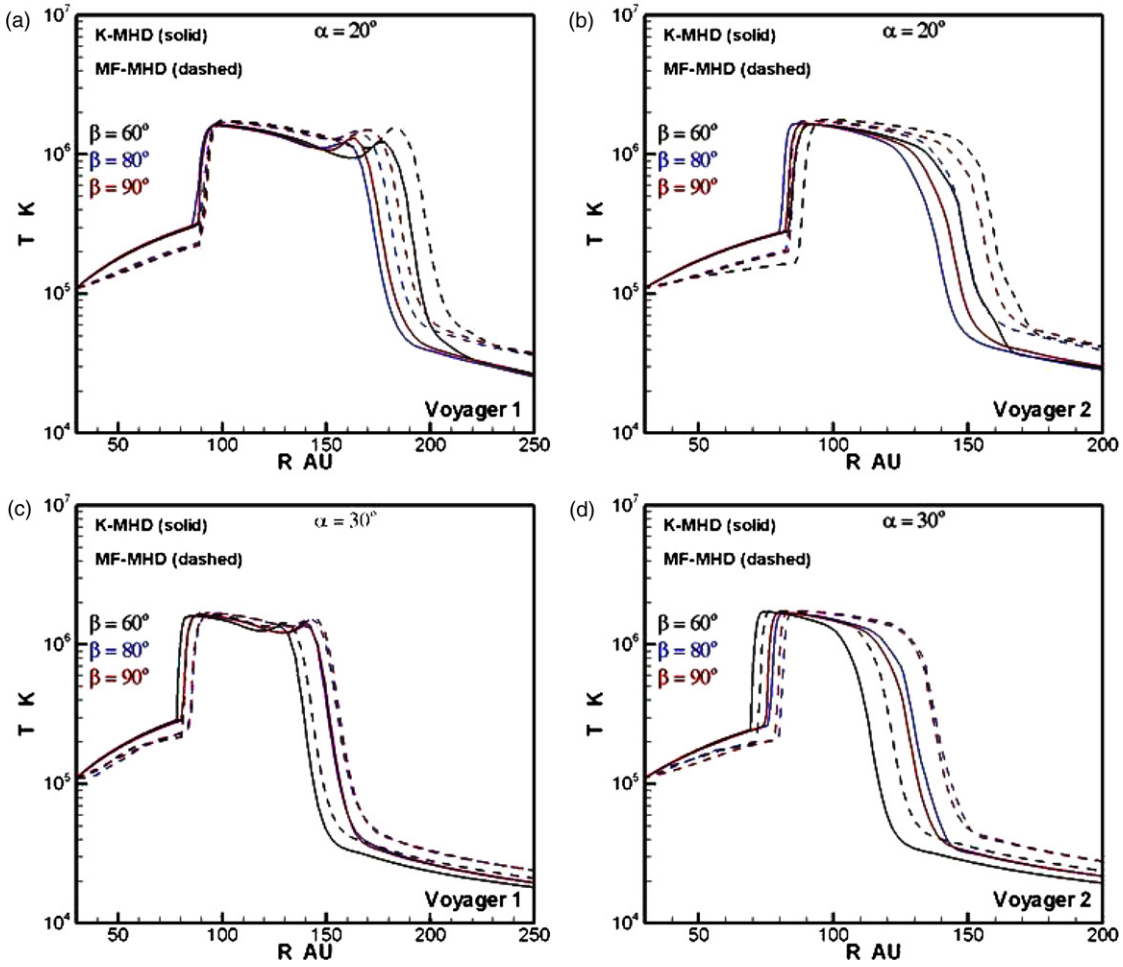

Figure 6. Plasma temperature profiles along *Voyager 1* and *Voyager 2* trajectories. Neutral hydrogen is accounted for using two models: multi-fluid (dashed lines) and kinetic (solid lines). The $B_{\rm LISM}$ intensity is 4.4 μG. Data along *V1* trajectory are shown in the left column, while the right column is for data along *V2* trajectory. The upper row is for the cases with ($\alpha = 20^\circ$, $\beta = 60^\circ$, 80°, 90°). The lower row is for ($\alpha = 30^\circ$, $\beta = 60^\circ$, 80°, 90°).

(A color version of this figure is available in the online journal.)

The density profiles (Figure 5) also show a net decrease in the mean heliosheath thickness $\langle L_{\rm HS}\rangle$ for the kinetic model, for all the considered cases of (α, β). The only exception has been the case of ($\alpha = 30^\circ$, $\beta = 80^\circ$), for which both models, i.e., kinetic and multi-fluid, gave similar values (~ 60 AU). The heliosheath thickness has the same trend as the TS; in that it has a greater dependence on α than on β. Moreover, both $\langle L_{\rm HS}\rangle$ and $\langle R_{\rm TS}\rangle$ are inversely proportional to α. This is simply the result that for smaller α, the ($V \times B$) force term outside the HP is small, thus a more expanded heliosheath. It is also worth mentioning that dependences on β are neither uniform nor preserved for different α.

The temperature profiles (Figure 6) show similar features at the heliospheric boundaries as for the density profiles. The heliosheath plasma is slightly cooler when neutrals are kinetic, which is the result of the increased rate of charge exchange with the shock heated solar wind. This is also confirmed by the strong deceleration of the heliosheath plasma in the kinetic model (see Figures 7(a) and (b)). The difference in the velocity profiles between the two models, for a given $B_{\rm LISM}$ configuration, extends to the region within the TS, especially for the case ($\alpha = 20^\circ$, $\beta = 60^\circ$). The temperature increase and velocity decrease within the TS boundary both point to a possible secondary charge-exchange process, whereby some of the neutrals that charge-exchanged in the heliosheath went through another charge-exchange process with the supersonic solar wind component, causing therefore not only the slowing down but a net heating of the solar wind.

The asymmetry of the TS between the *V1* and the *V2* crossing sites ($\Delta R_{{\rm TS}\_V1V2}$), is only slightly affected by the treatment of neutrals ($\Delta(\Delta R_{{\rm TS}\_V1V2})_{\rm Kinetic\_Multi\text{-}Fluid} \leqslant 1$ AU), the exception being ($\alpha = 20^\circ$, $\beta = 60^\circ$), in this case $\Delta(\Delta R_{{\rm TS}\_V1V2})_{\rm Kinetic\_Multi\text{-}Fluid} \sim 1.9$ AU (see Table 1). On average, accounting for all possible combinations of (α, β) in the chosen domain ($\alpha = 20^\circ$, 30° and $\beta = 60^\circ$, 80°, 90°), the TS asymmetry between *V1* and *V2* crossing sites ($\langle\Delta R_{{\rm TS}\_V1V2}\rangle$) is $\sim$6.9 AU for the kinetic model and $\sim$7 AU for the multi-fluid.

The deflection angle θ of the heliosheath flows, ($\theta = \tan^{-1}(V_N/V_T)$), is shown in Table 1. This angle expresses the ratio of the normal (V_N) and the tangential (V_T) velocity components downstream of the TS along *V2* trajectory. These velocity components (V_N, V_T) (Figures 7(a) and (b)) are calculated in the *RTN* spacecraft frame. Neutrals have a strong effect on the deflection angle, with the general trend of decreasing $|\theta|$ for the K-MHD model as compared to the MF-MHD model. The largest differences ($\Delta\theta = \theta_{\rm Kinetic} - \theta_{\rm MF}$) between the two models are attained for cases where ($\alpha = 20^\circ$). These differences vary from $\sim$4°.5 to $\sim 10^\circ$, with the maximum at ($\alpha = 20^\circ$, $\beta = 60^\circ$).

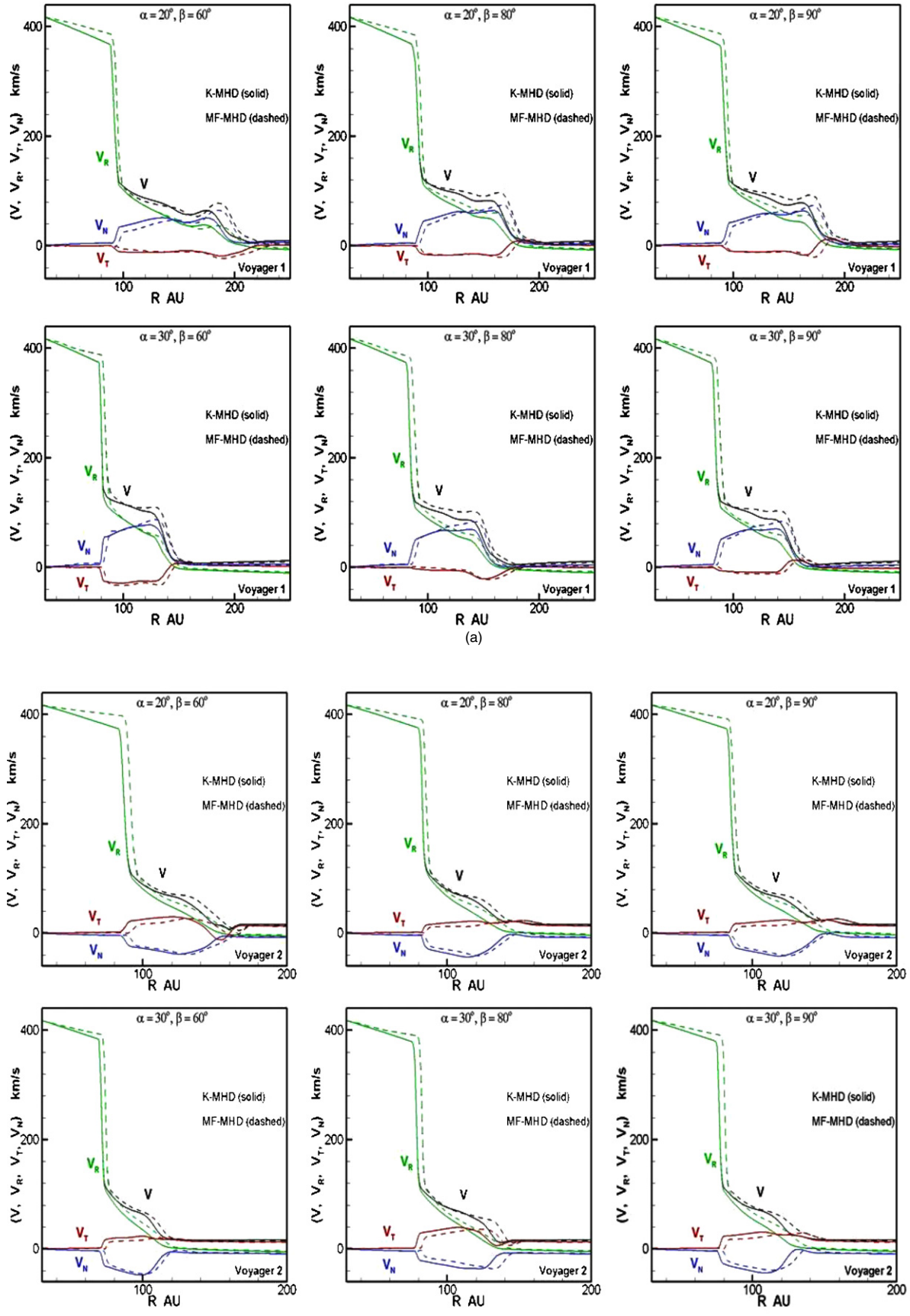

Figure 7. Plasma flow velocities (V, V_R, V_T, V_N) along the *Voyager* trajectories; (dashed lines) for the multi-fluid model and (solid lines) for the kinetic model. The $B_{\rm LISM}$ intensity is 4.4 μG. The upper row is for the cases with ($\alpha = 20^\circ$), and the lower row is for ($\alpha = 30^\circ$). (a) *V1* trajectory. (b) *V2* trajectory.
(A color version of this figure is available in the online journal.)

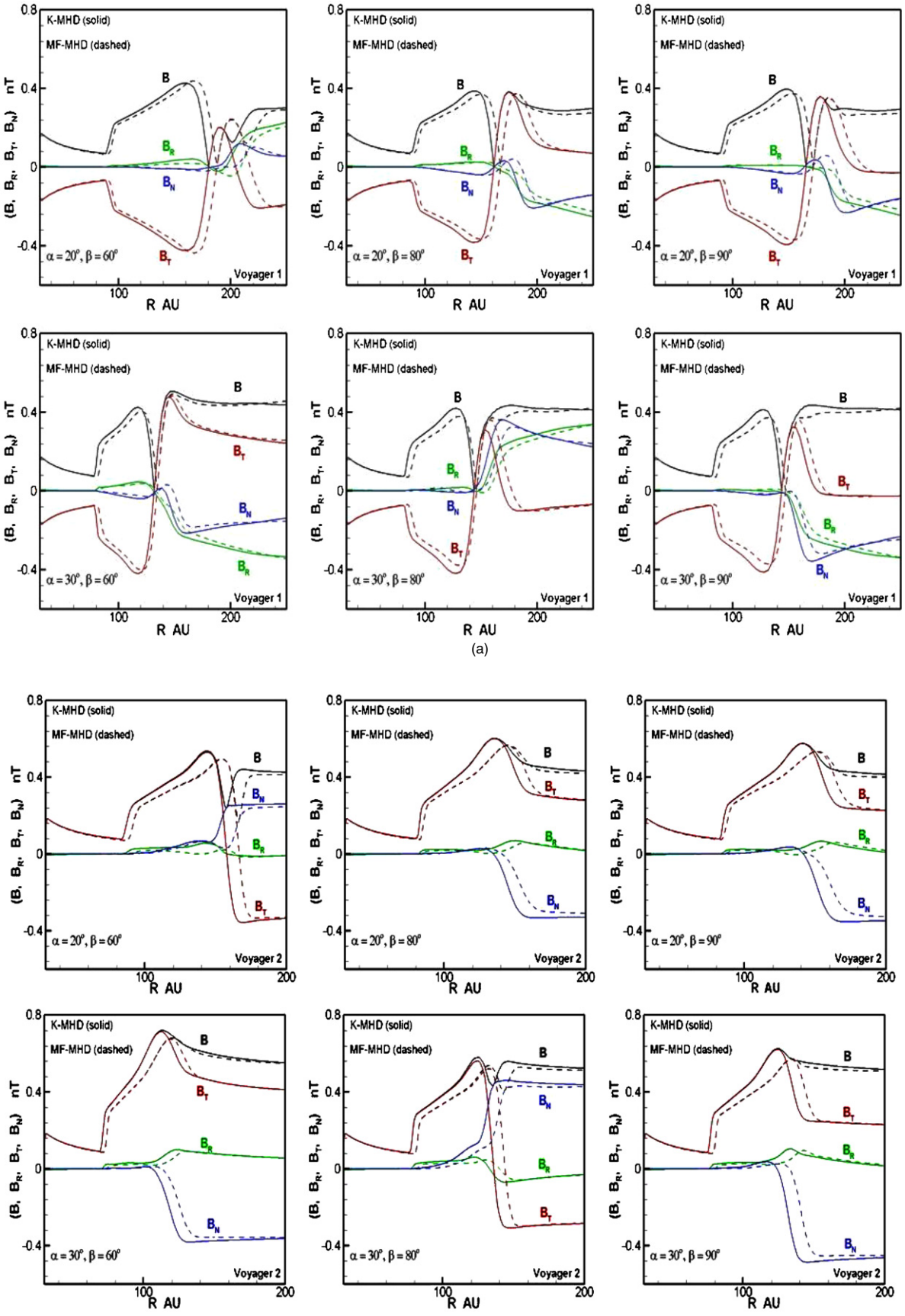

Figure 8. Magnetic field components (B, B_R, B_T, B_N) along the *Voyager* trajectories; (dashed lines) for the multi-fluid model and (solid lines) for the kinetic model. The $B_{\rm LISM}$ intensity is 4.4 μG. The upper row is for the cases with ($\alpha = 20^\circ$), and the lower row is for ($\alpha = 30^\circ$). (a) *V1* trajectory. (b) *V2* trajectory.
(A color version of this figure is available in the online journal.)

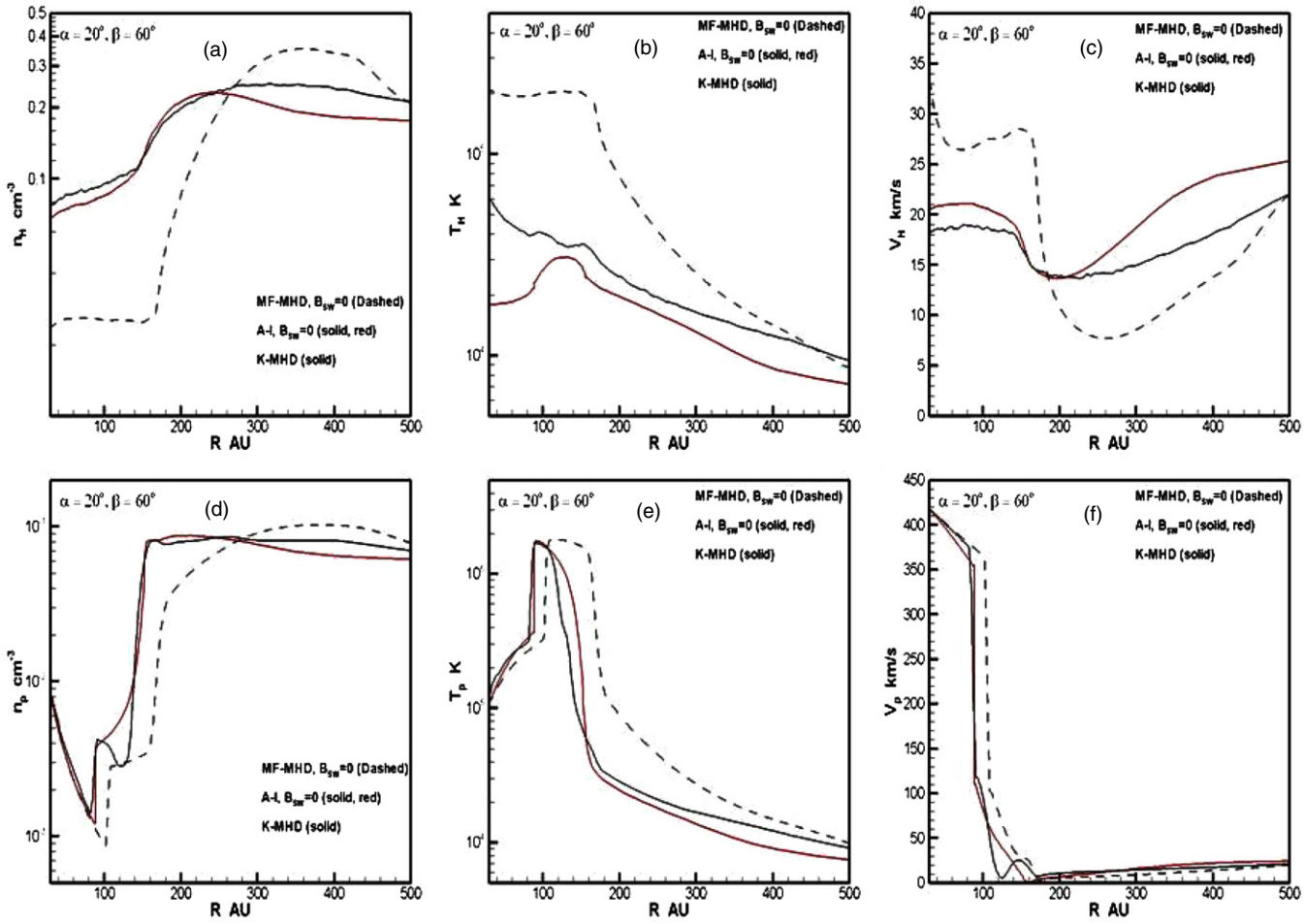

Figure 9. Neutral hydrogen and plasma density ((a) and (d)), temperature ((b) and (e)), and velocity ((c) and (f)) profiles, taken along the *X*-axis in upwind LISM flow direction. Dashed lines represent the MF-MHD model without the interplanetary magnetic field. Solid lines (in black) are data from the K-MHD model with a Parker solution for the interplanetary magnetic field at the inner boundary. Solid lines (in red) represent the Moscow University model A–I (Izmodenov et al. 2005; Alexashov & Izmodenov 2005) without any interplanetary magnetic field. The $B_{\rm LISM}$ intensity is 4.4 μG, with ($\alpha = 20^\circ$, $\beta = 60^\circ$).

(A color version of this figure is available in the online journal.)

For the cases where ($\alpha = 30^\circ$), $\Delta\theta$ varied between $\sim -1.2^\circ$ and $\sim 4.5^\circ$, where ($\alpha = 30^\circ$, $\beta = 80^\circ$) is the only case where the kinetic model showed a higher value of $|\theta|$. The detailed dependence of the deflection angle on the local interstellar magnetic field intensity and direction is shown in Opher et al. (2009). This study was done, however, using the multi-fluid model for neutrals.

The components of the magnetic field are shown in Figures 8(a) and (b) along *V1* (a) and *V2* (b). These profiles are expressed in the *RTN* spacecraft frame as in Figures 7(a) and (b). The *R*-axis is defined by the respective (*V1*) and (*V2*) heliocentric radius vectors. Because of the nature of the Parker field, the interplanetary field is mainly azimuthal upstream of the TS, i.e., along the *T* direction or e_Φ in spherical coordinates. Hence the overlap is between the total field (black curve) and the tangential field (red curve). Similar behavior is seen for the solar wind flow (Figures 7(a) and (b)), where upstream of the TS, the solar wind velocity is mainly radial. The deviation of the magnetic field from the Parker field takes place at the heliosheath, where the effect of the flow entrainment with the frozen-in field becomes important, at which point, the remaining components of the field, radial (B_R) and normal (B_N) to the spacecraft, mimic the behavior of the plasma flow (V_T and V_N). It is important to mention that the cancelation of the total magnetic field seen in Figure 8(a) along *V1* and the absence of such a feature in Figure 8(b) along *V2* is not a reconnection feature. This is simply due to the crossing of the current sheet, directed northward in our model, by the extrapolated *V1* trajectory. Magnetic reconnection, on the other hand, between the interstellar magnetic field and the interplanetary field can be expected locally at the HP (Swisdak et al. 2010), and can be a good candidate in explaining the 2–3 kHz radio signal near the HP (Gurnett et al. 2003).

The effect of the interplanetary field ($B_{\rm IP}$) on the plasma properties and the distribution of neutrals through the heliosphere is shown in Figure 9. Properties of ions and neutrals are compared between models, including the results from the A–I model (Izmodenov et al. 2005), which assumed ($B_{\rm IP} = 0$). The profiles shown in Figure 9 are taken along the *X*-axis upwind the LISM flow, which passes close to the HP stagnation point. The neutral density, temperature, and flow speed profiles (n_H, T_H, U_H) for the (MF-MHD) model are summed over all four neutral populations. This is done to facilitate the comparisons with the other two kinetic models. The main feature seen in Figure 9 is that for neutrals as well as for ions, the changes induced by the differences in models for neutrals, kinetic or multi-fluid, seem to dominate over any interplanetary field effect. This can be seen from the relative agreement between the K-MHD, $B_{\rm IP} \neq 0$

and the A–I, $B_{IP} = 0$ models. One needs to keep in mind that the steady-state solution of the highly supersonic solar wind interaction with the LISM depends mostly on the equilibrium between the solar wind ram pressure and the total LISM pressure. The interplanetary field pressure has a lesser role in the established equilibrium between these two winds. The presence of such a field, however, is crucial for the pick-up process of newly ionized neutrals inside the HP and the TS.

The observed decrease in the protons number density, for the K-MHD model, near the HP (Figure 9(d)) and the subsequent increase outside, is similar to what is seen in Figure 5. The reduction of solar wind ram pressure due to the increased filtration ratio leads to an unequal shift of both the TS and HP boundaries (Table 1). The non-uniformity in this shift is due to the relative differences in the charge-exchange rates within the heliosheath and inside the TS region, thus leading to a compression–rarefaction wave structure in the density profile. The reverse tendency is seen in the velocity profile (Figure 9(f)).

5. CONCLUSION

The kinetic model (K-MHD) of local interstellar hydrogen, more adequate in describing the transport of neutrals through the heliospheres, showed key differences in the heliospheric boundaries and the heliosheath flows with respect to the multi-fluid model (MF-MHD). Most important of these are the decrease of both the heliocentric distance to TS and the heliosheath thickness. The effect of the local interstellar magnetic field was assessed by varying the direction of the field using different combinations of the angles ($\alpha = 20°$, $30°$ and $\beta = 60°$, $80°$, $90°$) with a field intensity of 4.4 μG. The changes in heliospheric features for both kinetic and multi-fluid models revealed greater dependence on the angle α more than on β, making the former easier to constrain from observations.

The analysis of the deflection angle of the heliosheath flow (θ) showed a strong dependence on the neutral model. Lower deflections are achieved when neutrals are kinetic. These changes in θ across models imply that neutrals affect, in non-proportional way, the normal (V_N) and tangential (V_T) velocity components ($\theta = \tan^{-1}(V_N/V_T)$). This may be an indicator of anisotropy in the kinetic neutrals as they cross the HP. Nevertheless, the asymmetry of the TS is found to be the same for both models of neutrals (~6.9–7 AU).

The transport of neutrals through the heliosphere and the coupling with the solar wind protons seems to have a greater impact on the global features of the heliosphere than the interplanetary magnetic field. The absence of the interplanetary field, however, caused a reduction of some of the plasma properties within the TS boundary as shown by the A–I model.

The authors thank the staff at NASA Ames Research Center for the use of the Columbia supercomputer. This work was supported by the National Science Foundation Career Grant ATM-0747654 and NASA-*Voyager* Guest Investigator grant NNX07AH20G. D.A. was supported in part by RFBR grants 10-02-93113-НЦНИЛ_a and 10-01-00258-a. V.I. was supported in part by RFBR grant 10-02-01316-a, Dynastia foundation and the grant of President MD-3890.2009.2.

REFERENCES

Alexashov, D., & Izmodenov, V. V. 2005, A&A, 439, 1171
Allais, F., Matte, J-P., Alouani-Bibi, F., Kim, C. G., Stotler, D. P., & Rognlien, T. D. 2005, J. Nucl. Mater., 337, 246
Alouani-Bibi, F., Opher, M., Alexashov, D., Toth, G., & Izmodenov, V. V. 2010, AGU Fall Meeting, Abstract SH21A-1800
Axford, W. I. 1972, in Solar Wind, ed. Charles P. Sonett, Paul J. Coleman, & John M. Wilcox (NASA SP-308; Washington, DC: NASA), 609
Baranov, V. B. 1990, Space Sci. Rev., 52, 89
Baranov, V. B., & Malama, Y. G. 1993, J. Geophys. Res., 98, 15157
Bzowski, M. 2008, A&A, 488, 1057
Chalov, S. V., & Fahr, H. J. 2010, in AIP Conf. Proc 1216, Twelfth International Solar Wind Conf., ed. M. Maksimovic et al. (Melville, NY: AIP), 568
Gloeckler, G., et al. 2004, A&A, 426, 845
Gurnett, D. A., Kurth, W. S., & Stone, E. C. 2003, Geophys. Res. Lett., 30, 2209
Heerikhuisen, J., Florinski, V., & Zank, G. P. 2006, J. Geophys. Res., 111, A06110
Izmodenov, V. V. 2009, Space Sci. Rev., 143, 139
Izmodenov, V. V., Alexashov, D., & Myasnikov, A. 2005, A&A, 437, 35
Izmodenov, V. V., & Kallenbach, R. (ed.) 2006, The Physics of the Heliospheric Boundaries, ISSI Scientific Report (Paris: ESA-ESTEC)
Izmodenov, V. V., & Malama, Y. G. 2004, Adv. Space Res., 34, 74
Izmodenov, V. V., Malama, Y. G., Kalinin, A. P., Gruntman, M., Lallement, R., & Rodionova, I. P. 2000, Ap&SS, 274, 71
Izmodenov, V. V., Malama, Y. G., Ruderman, M. S., Chalov, S. V., Alexashov, D. B., Katushkina, O. A., & Provornikova, E. A. 2009, Space Sci. Rev., 146, 329
Lallement, R., Quemerais, E., Bertaux, J. L., Ferron, S., Koutroumpa, D., & Pellinen, R. 2005, Science, 307, 1447
Lallement, R., Quemerais, E., Koutroumpa, D., Bertaux, J. L., Ferron, S., Walter, S., & Lamy, P. 2010, in AIP Conf. Proc. 1216, Twelfth International Solar Wind Conf. (Melville, NY: AIP), 555
Linde, T. J., Gombosi, T. I., Roe, P. L., Powell, K. G., & DeZeeuw, D. L. 1998, J. Geophys. Res., 103, 1889
Lindsay, B. G., & Stebbings, R. F. 2005, J. Geophys. Res., 110, A12213
Linsky, J. L., & Wood, B. E. 1996, ApJ, 463, 254
Malama, Yu. G. 1991, ApS&S, 176, 21
Malama, Yu. G., Izmodenov, V. V., & Chalov, S. V. 2006, A&A, 445, 693
McComas, D. J., Elliott, H. A., Gosling, J. T., & Skoug, R. M. 2006, Geophys. Res. Lett., 33, L09102
McComas, D. J., et al. 2009, Science, 326, 959
McNutt, R. L., Jr., Lyon, J., & Goodrich, C. C. 1998, J. Geophys. Res., 103, 1905
Möbius, E., et al. 2004, A&A, 426, 897
Müller, H.-R., Zank, G. P., & Lipatov, A. S. 2000, J. Geophys. Res., 105, 27419
Myasnikov, A. V., Alexashov, D. B., Izmodenov, V. V., & Chalov, S. V. 2000, J. Geophys. Res., 105, 5179
Opher, M., Alouani-Bibi, F., Toth, G., Richardson, J. D., Izmodenov, V. V., & Gombosi, T. I. 2009, Nature, 462, 1036
Opher, M., Stone, E. C., & Gombosi, T. I. 2007, Science, 316, 875
Opher, M., Stone, E. C., & Liewer, P. C. 2006, ApJ, 640, L71
Parker, E. N. 1961, ApJ, 134, 20
Pauls, H. L., Zank, G. P., & Williams, L. L. 1995, J. Geophys. Res., 100, 21595
Pogorelov, N. V., Heerikhuisen, J., & Zank, G. P. 2008, ApJ, 675, L41
Pogorelov, N. V., Heerikhuisen, J., Zank, G. P., Mitchell, J. J., & Cairns, I. H. 2009, Adv. Space Res., 44, 1337
Powell, K. G., Roe, P. L., Linde, T. J., Gombosi, T. I., & DeZeeuw, D. L. 1999, J. Comput. Phys., 154, 284
Ratkiewicz, R., & Grygorczuk, J. 2008, Geophys. Res. Lett., 35, L23105
Stone, E. C., Cummings, A. C., McDonald, F. B., Heikkila, B. C., Lal, N., & Webber, W. R. 2005, Science, 309, 2017
Stone, E. C., Cummings, A. C., McDonald, F. B., Heikkila, B. C., Lal, N., & Webber, W. R. 2008, Nature, 454, 71
Swisdak, M., Opher, M., Drake, J. F., & Alouani-Bibi, F. 2010, ApJ, 710, 1769
Toth, G., et al. 2005, J. Geophys. Res., 110, A12226
Witte, M. 2004, A&A, 426, 835
Zank, G. P., & Pauls, H. L. 1996, Space Sci. Rev., 78, 95
Zank, G. P. 1999, Space Sci. Rev., 89, 413